Inorganic Chemistry
Article
pubs.acs.org/IC

New Monoclinic Phase at the Composition Cu_2SnSe_3 and Its Thermoelectric Properties

Jing Fan,[†,‡,§] Wilder Carrillo-Cabrera,[†] Lev Akselrud,[†] Iryna Antonyshyn,[†] Lidong Chen,[‡] and Yuri Grin*,[†]

[†]Max-Planck-Institut für Chemische Physik fester Stoffe, Nöthnitzer Strasse 40, 01187 Dresden, Germany

[‡]CAS Key Laboratory of Energy-Conversion Materials, Chinese Academy of Sciences, Shanghai Institute of Ceramics 1295 Dingxi Road, 200050 Shanghai, China

[§]University of Chinese Academy of Sciences, 19 Yuquan Road, 100049 Beijing, P. R. China

Supporting Information

ABSTRACT: A new monoclinic phase ($m2$) of ternary diamond-like compound Cu_2SnSe_3 was synthesized by reaction of the elements at 850 K. The crystal structure of $m2$-Cu_2SnSe_3 was determined through electron diffraction tomography and refined by full-profile techniques using synchrotron X-ray powder diffraction data (space group Cc, a = 6.9714(2) Å, b = 12.0787(5) Å, c = 13.3935(5) Å, β = 99.865(5)°, Z = 8). Thermal analysis and annealing experiments suggest that $m2$-Cu_2SnSe_3 is a low-temperature phase, while the high-temperature phase has a cubic crystal structure. According to quantum chemical calculations, $m2$-Cu_2SnSe_3 is a narrow-gap semiconductor. A study of the chemical bonding, applying the electron localizability approach, reveals covalent polar Cu−Se and Sn−Se interactions in the crystal structure. Thermoelectric properties were measured on a specimen consolidated using spark plasma sintering (SPS), confirming the semiconducting character. The thermoelectric figure of merit ZT reaches a maximum value of 0.33 at 650 K.

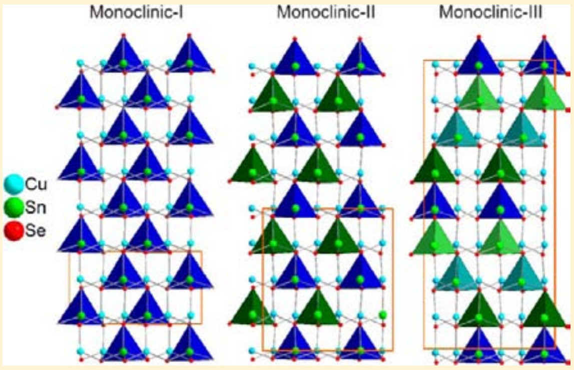

INTRODUCTION

The ternary chalcogenide semiconductor Cu_2SnSe_3 with diamond-like structure has attracted attention recently as a promising thermoelectric material,[1−6] due to its low thermal conductivity and tunable transport properties. A good figure of merit ZT of 1.14 at 850 K has been reported for an indium-doped sample $Cu_2In_{0.1}Sn_{0.9}Se_3$.[1] Through *ab initio* calculations, refs 1 and 7 suggested that the existence of a three-dimensional (3D) hole-like conductive network is probably responsible for the good thermoelectric performance of monoclinic-I Cu_2SnSe_3.

Diverse phases with cubic,[8−10] tetragonal,[11] or orthorhombic[12] crystal structure have been proposed for Cu_2SnSe_3. In particular, the most recently reported are two monoclinic structures, monoclinic-I ($m1$, space group Cc, a_1 = 6.9670(3) Å, b_1 = 12.0493(7) Å, c_1 = 6.9453(3) Å, β_1 = 109.19(1)°)[13] and monoclinic-III ($m3$, space group Cc, a_3 = 6.9612(14) Å, b_3 = 12.043(2) Å, c_3 = 26.481(5) Å, β_3 = 94.97(3)°).[14] Different preparation conditions and compositions may lead to this variety of results. Unfortunately, most of the publications do not provide specific compositions, limiting the detailed judgment about the composition−structure relationship for Cu_2SnSe_3. Furthermore, only the structure of the monoclinic-III phase is determined from single-crystal diffraction data while the other structures are determined from powder X-ray diffraction data. The superstructure reflections and splitting of the main reflections allowing a distinction between these phases can be easily overlooked in standard laboratory-collected powder X-ray diffraction data. Since this may result in an inappropriate assignment of the space group or unit cell, the present knowledge of the various structures of the phases around the composition Cu_2SnSe_3 is unsatisfying.

For a better understanding of the properties of Cu_2SnSe_3, especially to provide a good starting model for theoretical calculations of its electronic band structure and chemical bonding, it is mandatory to determine precisely the crystal structure of the phases around the composition Cu_2SnSe_3 and the conditions of their formation. For this purpose, we employed electron diffraction tomography method. This is a novel technique for reflection intensity data acquisition intended for ab initio structure determination of phases using only 100−400 nm size crystals.[15] Recently, this technique was successfully employed for the crystal structure redetermination of the complex phase $BaGe_5$.[16,17]

In this study, Cu_2SnSe_3 with stoichiometric composition is prepared through carefully controlling the synthesis conditions. The crystal structure of the monoclinic-II modification $m2$-

Received: May 26, 2013
Published: September 18, 2013

Cu_2SnSe_3 is solved through electron diffraction tomography analysis, and then refined by the Rietveld refinement using high resolution synchrotron X-ray powder diffraction data. A comparison with the monoclinic-I and monoclinic-III modifications is given. The thermal behavior and the thermoelectric properties are also reported.

■ EXPERIMENTAL SECTION

Sample Preparation. A polycrystalline sample of nominal composition Cu_2SnSe_3, named hereafter *m2*-Cu_2SnSe_3, was prepared by direct reaction of stoichiometric mixture of the elements Cu (powder, 99.999%, Chempur), Sn (foil, 99.99%, Chempur), and Se (shot, 99.999%, Alfa Aesar) in an evacuated fused quartz ampule at 1173 K for 12 h, cooled down to 850 K in 24 h, annealed at this temperature for 7 days, and finally quenched in cold water. To prove the transformation to the high-temperature phase, a second sample was annealed at 950 K for comparison, with the further conditions maintained exactly the same.

The *m2*-Cu_2SnSe_3 sample was ground into fine powder and cold pressed into pellets. To ensure homogeneity, it was then annealed at 850 K for another 7 days. In order to obtain densified bulk specimens suitable for thermoelectric property measurements, the reground powder was subjected to spark plasma sintering (SPS, SPS-515 ET/M apparatus, Synthex Ltd., Tokyo). Consolidation was performed by heating to 790 at 25 K/min under a uniaxial pressure of 60 MPa. This temperature was held for 10 min. The density of the pellet, determined by Archimedes method, was >98% of its theoretical value.

Electron Diffraction Tomography. Conventional transmission electron microscopy (TEM) and manually controlled electron diffraction tomography were performed on the *m2*-Cu_2SnSe_3 sample applying a FEI TECNAI 10 (100 kV) microscope, equipped with a 2k CCD camera (TemCam-F224HD, TVIPS). The selected area electron diffraction (SAED) mode was used for data collection. A thin crystal (thickness ca. 60 nm) on a holey carbon-coated TEM support grid was chosen for data acquisition. The crystal area selected for electron diffraction filled almost the full aperture area (diameter of about 450 nm, Figure 4a). The tilt sequence at steps of 1° was performed manually in a total tilt range from −60° to 49° using a standard double-tilt holder (GATAN). The collected series data were stored as a set of files in TIF format, converted into MRC format stacks, and further processed for reconstruction of the diffraction volume, using the ADT3D software package.[15] After indexing the spots in the reciprocal-space lattice, the intensities were integrated and stored as standard *hkl* file (559 reflections measured, 456 symmetry-independent reflections).

Laboratory X-ray Powder Diffraction. X-ray powder diffraction experiments were carried out on a Huber image plate Guinier camera G670 (Cu $K\alpha_1$ radiation, λ = 1.540 60 Å, germanium (111) monochromator, 6 × 30 min scans, $3° \leq 2\theta \leq 100.3°$) at ambient temperature. The lattice parameters were refined using Si (a = 5.4312 Å) as internal standard, with a least-squares technique, employing the WinCSD program package.[18]

Synchrotron X-ray Powder Diffraction. For a high-resolution synchrotron powder diffraction experiment, *m2*-Cu_2SnSe_3 powder with particle size between 20 and 50 μm was filled in a quartz capillary (ϕ = 0.5 mm) and sealed under Ar atmosphere. The data were collected at the high-resolution beamline ID31 of the European Synchrotron Radiation Facility (ESRF) in Grenoble, which was equipped with a multianalyzer stage with nine detectors each preceded by a Si(111) crystal (Debye−Scherrer geometry, λ = 0.430 46 Å, scan step of 0.001°, $1° \leq 2\theta \leq 44°$). Rietveld refinement was performed employing the WinCSD program package. Details concerning the data collection and structure refinement are given in Table 1. Finally, the PLATON software was used to prove for additional symmetry (ADDSYM module).[19]

Chemical Analysis. Chemical analyses were carried out on *m2*-Cu_2SnSe_3 annealed sample and on the pellet obtained after SPS. Inductively coupled plasma atomic emission spectroscopy (ICP-AES, Varian Vista RL) was utilized for the total composition analysis. The local chemical composition has been determined by wavelength-dispersive X-ray spectroscopy (WDXS, Cameca SX100). The intensities of the X-ray lines Cu $K\alpha$, Sn $L\alpha$, and Se $K\alpha$ were determined with focusing monochromator crystals of LiF (lithium fluoride) and PET (pentaerythritol). An electron beam 15 nA/25 kV was adjusted for Cu $K\alpha$ and Se $K\alpha$ lines. For the excitation of the Sn $L\alpha$ line an electron beam 25 nA/25 kV was used. Averaging on 10 points and the φ(Fz)-matrix correction model were applied. Elemental Cu, Sn, and Se have been used as references.

Table 1. Crystallographic Data for *m2*-Cu_2SnSe_3

formula; molar mass	Cu_2SnSe_3; 482.65 g mol^{-1}
cryst syst; space group	monoclinic; *Cc* (No. 9)
a, b, c/Å (powder data)	6.9714(2), 12.0787(5), 13.3935(5)
β/deg (powder data)	99.865(5)
unit cell volume/Å^3 (powder data)	1111.13(7)
Z; ρ_c/(g cm^{-3})	8; 5.77
diffractometer	nine-crystal multianalyzer stage
λ/Å; monochromator	0.430 46 ; Si 111 crystal
T/K	295
2θ range/deg	3 to 33
μ/mm^{-1}	9.59
F(000)/e	1680
reflns in measured range	1336
refined params	84
refinement method	full-profile Rietveld
R_I; R_p; R_{wp}	0.060, 0.103, 0.156

Thermal Analysis. Differential thermal analysis and thermogravimetric analysis (DTA/TG) were performed on a Netzsch STA 449C in the temperature range 300−1023 K with a heating rate of 10 K/min, under Ar atmosphere. The sample was loaded in an Al_2O_3 crucible.

Thermoelectric Properties. The thermal diffusivity λ was measured on the disk-shaped specimen using a laser-flash technique employing a Netzsch LFA 427 setup in the temperature range from 300 to 700 K in He atmosphere. The thermal conductivity κ was then calculated as $\kappa = C_p d\lambda$, where d is the density and C_p is the Dulong−Petit approximation for the specific heat capacity. For the electrical transport properties measurement, a bar-shaped specimen of 1.5 × 1.5 × 10 mm^3 was cut with a diamond wire saw from the disk-shaped specimen. Both electrical resistivity ρ and Seebeck coefficient S were determined simultaneously (ULVAC-RIKO ZEM-3) in the temperature range from 300 to 700 K in He atmosphere.

Calculation Procedures. Electronic structure calculation and bonding analysis were carried out for *m2*-Cu_2SnSe_3 using the lattice parameters and atomic positions from the crystal structure determination (Tables 1 and 2). The TB-LMTO-ASA program

Table 2. Atomic Coordinates and Isotropic Displacement Parameters (in Å^2) for *m2*-Cu_2SnSe_3

atom	site	x	y	z	U_{eq}[a]
Cu1	4*a*	−0.0023(8)	0.0824(4)	0.7595(4)	0.013
Cu2	4*a*	−0.0093(7)	0.2480(3)	0.2542(4)	0.013
Cu3	4*a*	0.2367(7)	−0.0818(4)	0.0059(3)	0.013
Cu4	4*a*	0.7464(7)	0.0864(3)	0.0049(3)	0.013
Sn1	4*a*	0.2500(3)	0.2500(2)	0.0000(2)	0.013
Sn2	4*a*	−0.0018(7)	0.4204(2)	0.7542(3)	0.013
Se1	4*a*	0.0446(6)	0.0817(4)	−0.0577(3)	0.013
Se2	4*a*	0.0495(5)	0.4255(4)	−0.0505(3)	0.013
Se3	4*a*	0.3015(6)	0.2541(3)	0.1953(3)	0.013
Se4	4*a*	0.5704(6)	0.2561(4)	−0.0572(3)	0.013
Se5	4*a*	0.3050(6)	0.0927(4)	0.6920(4)	0.013
Se6	4*a*	0.3261(6)	0.4210(4)	0.6921(3)	0.013

[a] All atoms were constrained to have same isotropic displacement parameter.

package was employed.[20] The Barth–Hedin exchange potential[21] was used for the LDA calculations. The radial scalar-relativistic Dirac equation was solved to obtain the partial waves. Though the calculation within the atomic sphere approximation (ASA) includes corrections for the neglect of interstitial regions and partial waves of higher order,[22] an addition of empty spheres was necessary for structural reasons: the packing of tetrahedrons contains large voids (Figure 7). The following radii of the atomic spheres were applied for the calculations: $r(\text{Cu1}) = 1.330$ Å, $r(\text{Cu2}) = 1.365$ Å, $r(\text{Cu3}) = 1.355$ Å, $r(\text{Cu4}) = 1.331$ Å, $r(\text{Sn1}) = 1.509$ Å, $r(\text{Sn2}) = 1.544$ Å, $r(\text{Se1}) = 1.469$ Å, $r(\text{Se2}) = 1.500$ Å, $r(\text{Se3}) = 1.483$ Å, $r(\text{Se4}) = 1.424$ Å, $r(\text{Se5}) = 1.452$ Å, $r(\text{Se6}) = 1.480$ Å. For each calculation, a basis set containing Cu(4*s*,4*p*,3*d*), Sn(5*s*,5*p*), and Se(4*s*,4*p*) orbitals was employed for a self-consistent calculation with Sn(5*p*,4*f*) and Se(4d) functions being down-folded.

The electron localizability indicator (ELI, γ) was evaluated in the ELI-D representation according to refs 23–25 with an ELI-D module within the program package TB-LMTO-ASA.[20] Topological analysis of the electron density, i.e., estimation of the shapes, volumes, and charges of the atoms after Bader (QTAIM atoms),[26] and of the electron localizability indicator, e.g., localization of the ELI maxima as fingerprints of the direct covalent atomic interactions, was performed with the program DGrid.[27]

■ RESULTS AND DISCUSSION

Thermal Behavior and Crystal Structure. The strongest endothermic peak at 964 K in the DTA curve of *m2*-Cu_2SnSe_3 sample (Figure 1) reveals the melting point in good agreement with the values between 958 and 970 K reported in the literatures.[12,28–30] A weak endothermic peak at 930 K indicates a phase transition.

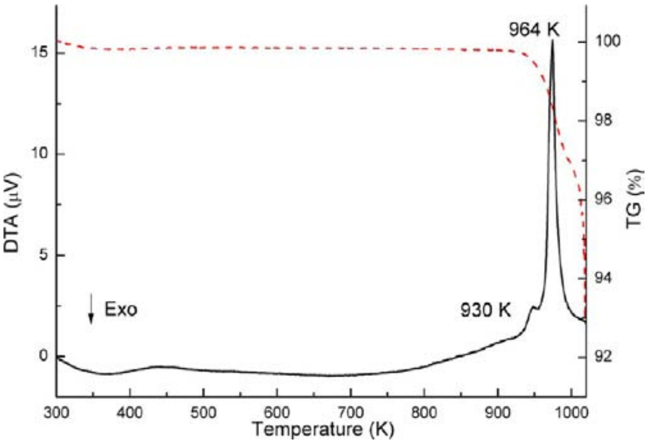

Figure 1. Thermal behavior of *m2*-Cu_2SnSe_3 sample (heating rate 10 K/min). The black solid line is the DTA curve, and the red dashed line is the TG curve.

The X-ray powder diffraction pattern of Cu_2SnSe_3 samples annealed at 850 and 950 K mainly differ in some low-intensity superstructure reflections (Figure 2). Our following analysis shows that the *m2*-Cu_2SnSe_3 sample annealed at 850 K crystallizes in a new monoclinic structure. The sample obtained at 950 K crystallizes in the cubic sphalerite-type structure, indicated by the appearance of only the strong reflections (111), (022), (113), (004), (133), (224), and (115). Several small very broad peaks may originate from monoclinic phase with low crystallinity, probably because the quenching process was not quick enough or the annealing time was not long enough to finish the structural transformation. Therefore, the monoclinic-II modification is a low-temperature phase, and the cubic modification is a high-temperature phase of Cu_2SnSe_3.

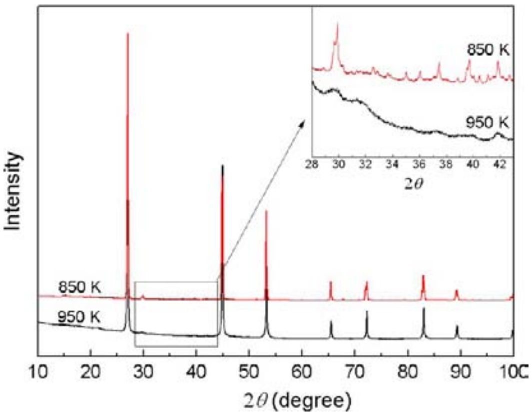

Figure 2. X-ray powder diffraction patterns of the *m2*-Cu_2SnSe_3 sample annealed at 850 and 950 K. Weak reflections from selected angle area distinguishing the two samples are shown in the inset.

The *m2*-Cu_2SnSe_3 phase crystallizes forming twinned domains (Figure 3); therefore, it was difficult to find individual single crystal of high quality with size suitable for X-ray single-crystal analysis. We then resorted to electron diffraction tomography method which could be used to analyze nano-crystallites. The electron diffraction tomography study suggested a *C*-centered monoclinic unit cell (for all observed reflections *hkl*, $h + k = 2n$) for the *m2*-Cu_2SnSe_3 sample. The resulting unit cell parameters are $a = 6.93$ Å, $b = 12.12$ Å, $c = 13.39$ Å, $\alpha = 90.36°$, $\beta = 99.79°$, $\gamma = 89.31°$. The final lattice parameters listed in Table 1 are obtained from powder X-ray diffraction data. Further reflection conditions were deduced from the SAED diffraction patterns in Figure 4: $h0l$, h, $l = 2n$; $h00$, $h = 2n$; $00l$, $l = 2n$ (Figure 4c); $0kl$, $k = 2n$ (Figure 4b). In contrast to Figure 4c, the reflection condition $00l$, $l = 2n$ is not satisfied in the SAED pattern in Figure 4b. This is probably due to dynamical effects (double reflection) along [100] direction. Without taking into account the dynamical effects, the analysis suggested the space groups $C2/c$ or Cc. Given the fact that this phase is a superstructure of the cubic phase (space group $F\bar{4}3m$, $a_c = 5.688–5.696$ Å[8–10]), which is noncentrosymmetric, finally the noncentrosymmetric space group Cc was chosen. The structure solution was achieved by direct methods using the SIR2011 software,[31] and the atom positions were further refined with the SHELXL software.[32] The final *R*-value was large ($R_1 = 0.32$; 418 reflections, 37 refined parameters), but still reasonable for electron diffraction data without corrections (absorption and residual dynamical effects). Figure 5 displays the projections of 3D diffraction patterns for *m2*-Cu_2SnSe_3 in three different directions.

On the basis of the model suggested by electron diffraction tomography, full-profile refinement of the crystal structure of *m2*-Cu_2SnSe_3 was carried out employing the high-resolution synchrotron X-ray powder diffraction data. In addition to the main monoclinic phase (85.56 mass %), two minority phases were found: cubic Cu_2SnSe_3 (9.77 mass %) and tetragonal Cu_2SnSe_3 (4.67 mass %), as shown in Figure 6. The space group $I\bar{4}2d$ and the crystal structure of the chalcopyrite type ($a = 5.6968(1)$ Å, $c = 11.4257(2)$ Å) were assumed for the tetragonal phase. Since the correlation of parameters is strong and free refinement of the displacement parameters was unstable, all the atoms were constrained to have equal isotropic

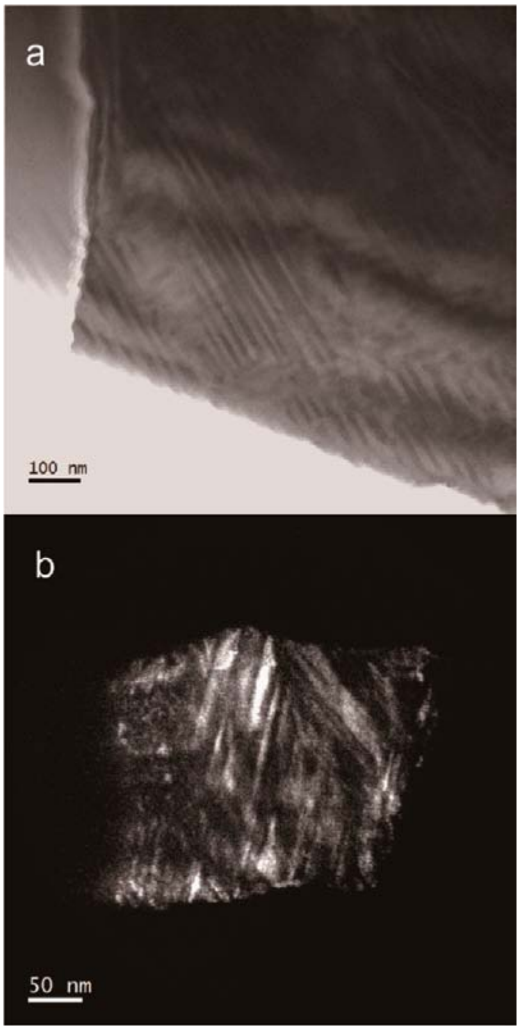

Figure 3. Defects observed in *m2*-Cu_2SnSe_3: (a) bright field TEM image of a particle with twin domains of about 10 nm size; (b) dark field TEM image of another particle with twin domains (about 10−20 nm size) oriented in two directions.

displacement parameter. The final atomic coordinates and displacement parameters for *m2*-Cu_2SnSe_3 are summarized in Table 2. The program ADDSYM in the PLATON package suggested no additional symmetry. Moreover, an attempt to refine the data with centrosymmetric space group *C*2/*c* was also performed, but several split positions occupied by 50% had to be applied for Se atoms, strongly indicating a wrong choice of the space group. Table 3 shows the selected interatomic distances and angles within the cation-centered selenium tetrahedra. The Cu−Se distances range from 2.355(6) to 2.491(6) Å, and the Sn−Se distances range from 2.484(5) to 2.580(5) Å. Those values agree well with the distances found in the monoclinic-III Cu_2SnSe_3: Cu−Se and Sn−Se distances are 2.380(5)−2.495(5) Å and 2.488(3)−2.627(3) Å, respectively.[14] The total composition $Cu_{2.01(1)}Sn_{1.01(1)}Se_{2.99(1)}$ of the *m2*-Cu_2SnSe_3 sample established by ICP-AES technique and the local composition $Cu_{2.00(1)}Sn_{1.00(1)}Se_{3.00(1)}$ evaluated by WDX spectroscopy confirmed well the stoichiometric composition assumed for the structure solution and refinement.

Since the new modification *m2*-Cu_2SnSe_3 exhibits a unit cell volume in-between the two monoclinic modifications reported earlier, we call it as monoclinic-II. All three monoclinic modifications of Cu_2SnSe_3 are superstructures to the cubic sphalerite-type structure. The structural pattern is characterized by tetrahedral coordination of atoms. Cu and Sn are each coordinated by four Se atoms, forming a three-dimensional network of corner-sharing MSe_4 tetrahedra (M = Cu or Sn). Though Cu and Sn are disordered in the cubic Cu_2SnSe_3, they are ordered distinctively in the monoclinic variants. A common feature in these monoclinic structures is that one-third of the Se atoms are coordinated by two Cu and two Sn, and two-thirds of the Se atoms are coordinated by three Cu and one Sn. In this way the Cu_3Sn and Cu_2Sn_2 coordination around Se are two environments satisfying the octet rule.[33,34] All three monoclinic structures of Cu_2SnSe_3 have practically the same *a* and *b* axes ($a_i = \sqrt{6}/2a_c$, $b_i = ((3\sqrt{2})/2)a_c$, $i = 1, 2, 3$, a_c stands for the lattice parameter of the cubic sphalerite-like unit cell). However, the distinct Sn/Cu ordering generates different zigzag chains of Sn-centered tetrahedrons (Figure 7) and, consequently, different but related *c*-axis lengths: $c_1 = \sqrt{6}/2a_c$, $c_2 = \sqrt{6}a_c$, $c_3 = \sqrt{6}a_c$. As a result, the X-ray powder diffraction patterns for these three Cu_2SnSe_3 structure are extremely similar, and the differences manifest only in additional low-intensity superstructure reflections and distinct splitting of the main reflections.

Studying systematically ternary chalcogenides in the Cu−Sn−Se system, we were only able to obtain monoclinic-III phase samples in a narrow Sn-rich composition range. Attempts to prepare the monoclinic-I phase have so far been not successful.

Electronic Structure and Chemical Bonding. The electronic density of states (DOS) of *m2*-Cu_2SnSe_3 (Figure 8) is in general similar to that previously reported for the monoclinic-I crystal structure.[1,7,33] Below the Fermi level, DOS

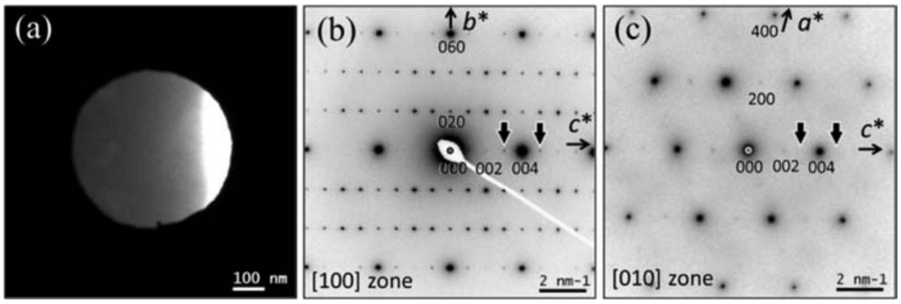

Figure 4. (a) Area of an *m2*-Cu_2SnSe_3 crystal (thickness about 60 nm, aperture radius ca. 220 nm) used for electron diffraction tomography, and selected area diffraction patterns (SAED) of Cu_2SnSe_3 along (b) [100] and (c) [010]. The reflections marked by thick black arrows in b, i.e., 003 and 005, appear due to dynamical effects (not present in c).

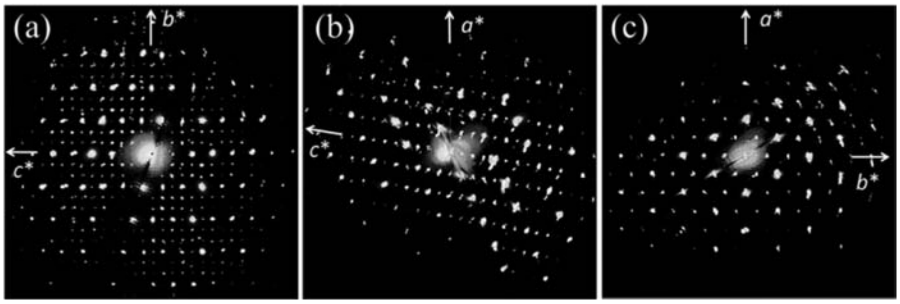

Figure 5. Projections of 3D diffraction pattern (reciprocal volume) for *m2*-Cu_2SnSe_3 along [100] (a), [010] (b), and [001] (c) directions. Additional reflections originate from crystal satellites.

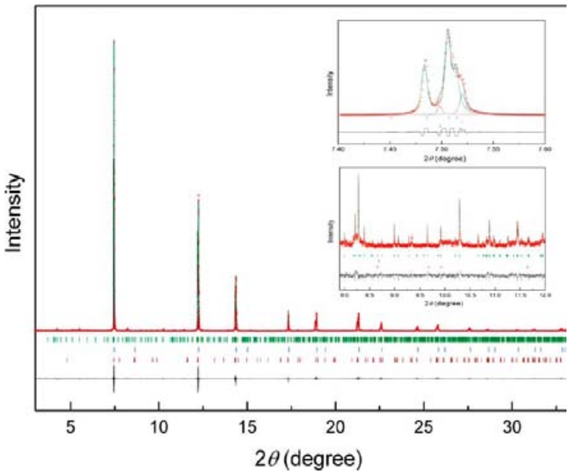

Figure 6. Synchrotron X-ray powder diffraction pattern of the *m2*-Cu_2SnSe_3 sample at 295 K (red dots) with the calculated profile (black line) after Rietveld refinement. Bragg peaks of the monoclinic, cubic, and tetragonal Cu_2SnSe_3 phases are marked with green, blue, and brown vertical bars, respectively. The difference curve $Y_{obs} - Y_{calc}$ is shown at the bottom of the plot. The insert shows magnifications of the strongest reflection and the superstructure reflections between 7.9 and 12°.

Table 3. Selected Bond Lengths (Å) and Angles (deg) for *m2*-Cu_2SnSe_3[a]

Cu1–Se6^{i}	2.382(7)	Se6^{i}–Cu1–Se1^{ii}	110.67(2)
Cu1–Se1^{ii}	2.412(6)	Se6^{i}–Cu1–Se5	108.27(2)
Cu1–Se5	2.467(7)	Se6^{i}–Cu1–Se3^{iii}	108.05(2)
Cu1–Se3^{iii}	2.469(6)	Se1^{ii}–Cu1–Se5	113.36(2)
		Se1^{ii}–Cu1–Se3^{iii}	109.07(2)
		Se5–Cu1–Se3^{iii}	107.24(2)
Cu2–Se5^{iv}	2.387(6)	Se5^{iv}–Cu2–Se6^{iv}	111.32(2)
Cu2–Se6^{iv}	2.418(6)	Se5^{iv}–Cu2–Se3	108.81(2)
Cu2–Se3	2.430(7)	Se5^{iv}–Cu2–Se4^{v}	112.55(2)
Cu2–Se4^{v}	2.491(6)	Se6^{iv}–Cu2–Se3	108.14(2)
		Se6^{iv}–Cu2–Se4^{v}	109.96(2)
		Se3–Cu2–Se4^{v}	105.81(2)
Cu3–Se4^{i}	2.355(6)	Se4^{i}–Cu3–Se2^{vi}	109.33(2)
Cu3–Se2^{vi}	2.429(6)	Se4^{i}–Cu3–Se1	109.72(2)
Cu3–Se1	2.456(6)	Se4^{i}–Cu3–Se5^{vii}	108.55(2)
Cu3–Se5^{vii}	2.459(6)	Se2^{vi}–Cu3–Se1	109.09(2)
		Se2^{vi}–Cu3–Se5^{vii}	106.82(2)
		Se1–Cu3–Se5^{vii}	113.24(2)
Cu4–Se1^{viii}	2.372(6)	Se1^{viii}–Cu4–Se2^{vi}	110.92(2)
Cu4–Se2^{vi}	2.421(6)	Se1^{viii}–Cu4–Se4	108.43(2)
Cu4–Se4	2.460(6)	Se1^{viii}–Cu4–Se6^{ix}	107.46(2)
Cu4–Se6^{ix}	2.475(6)	Se2^{vi}–Cu4–Se4	109.93(2)
		Se2^{vi}–Cu4–Se6^{ix}	107.36(2)
		Se4–Cu4–Se6^{ix}	112.73(2)
Sn1–Se4	2.484(5)	Se4–Sn1–Se1	114.9(2)
Sn1–Se1	2.529(5)	Se4–Sn1–Se2	111.8(1)
Sn1–Se2	2.565(4)	Se4–Sn1–Se3	109.7(2)
Sn1–Se3	2.580(5)	Se1–Sn1–Se2	109.2(1)
		Se1–Sn1–Se3	107.4(2)
		Se2–Sn1–Se3	103.1(1)
Sn2–Se5^{x}	2.539(5)	Se5^{x}–Sn2–Se6	110.08(2)
Sn2–Se6	2.563(6)	Se5^{x}–Sn2–Se3^{iii}	110.35(2)
Sn2–Se3^{iii}	2.564(5)	Se5^{x}–Sn2–Se2^{ii}	106.67(2)
Sn2–Se2^{ii}	2.578(5)	Se6–Sn2–Se3^{iii}	111.22(2)
		Se6–Sn2–Se2^{ii}	110.61(2)
		Se3^{iii}–Sn2–Se2^{ii}	107.78(2)

[a] Symmetry codes: (i) −0.5 + *x*, −0.5 + *y*, *z*; (ii) *x*, *y*, 1 + *z*; (iii) −0.5 + *x*, 0.5 − *y*, 0.5 + *z*; (iv) −0.5 + *x*, 0.5 − *y*, −0.5 + *z*; (v) −0.5 + *x*, 0.5 − *y*, *z*; (vi) 0.5 + *x*, −0.5 + *y*, *z*; (vii) *x*, −*y*, −0.5 + *z*; (viii) 1 + *x*, *y*, *z*; (ix) 0.5 + *x*, 0.5 − *y*, −0.5 + *z*; (x) −0.5 + *x*, 0.5 + *y*, *z*.

consists of four well separated regions. The low-energy range ($E < -9$ eV) is composed mainly of Se(*s*) states with minor participation of other states, which may indicate rather a lone-pair character of the Se(*s*) states. The DOS around −8 eV is formed mainly by Sn(*s*) states, with admixtures of other states which are in general small but definitely larger than these observed for the low-energy region. Thus, the Sn(*s*) states show a more bonding character than the *s* states of Se. The DOS region below the Fermi level is split in two parts and formed predominantly by the Se(*p*) and Cu(*d*) states. In the range -6.5 eV $< E < -3$ eV, the Cu(*s*) and Sn(*p*) states are also contributing to the total DOS, whereas the region immediately below the Fermi level (-3 eV $< E < E_F$) is formed additionally by the Sn(s) and Sn(p) contributions. The electronic DOS of *m2*-Cu_2SnSe_3 reveals a narrow band gap of 0.1 eV and indicates semiconducting behavior, assuming the ideal composition.

Further insight into the organization of the crystal structure was obtained applying the analysis of atomic interactions in real space within the electron localizability approach.[27] From chemical intuition, the interaction between the Cu and Sn on the one hand, and Se on the other, may be expected as an ionic one described by the balance $Cu^{1+}{}_2Sn^{4+}Se^{2-}{}_3$. In such case the Cu and Sn atoms fully deliver their valence electrons in order to fulfill the octet rule of Se. The integration of the electron density within the atomic basins in accordance with the quantum theory of atoms in molecules (QTAIM[33]) yields effective charges being rather small in respect to the ionic balance above: $Cu1^{0.20+}$, $Cu2^{0.21+}$, $Cu3^{0.31+}$, $Cu4^{0.29+}$, $Sn1^{1.18+}$, $Sn2^{1.12+}$, $Se1^{0.67-}$, $Se2^{0.48-}$, $Se3^{0.47-}$, $Se4^{0.51-}$, $Se5^{0.56-}$, and $Se6^{0.63-}$. In accordance with the electronegativities of the constituting

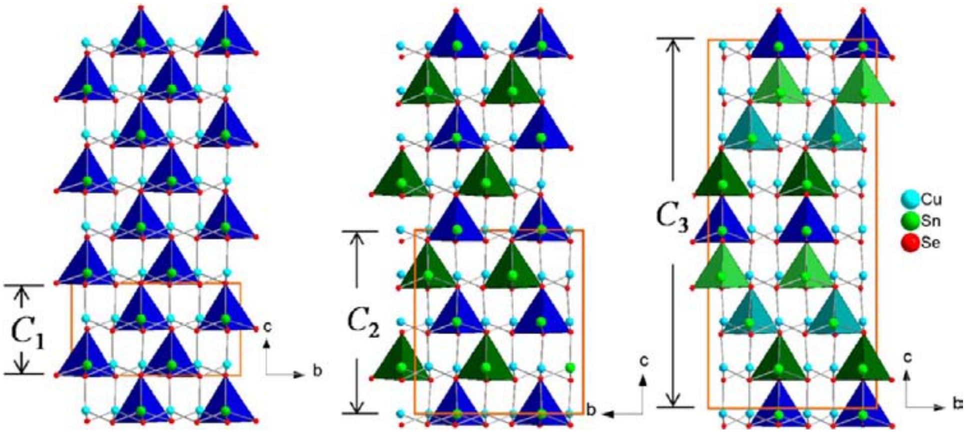

Figure 7. Packing of the Sn-centered tetrahedra in the monoclinic modifications of Cu_2SnSe_3: I (left), II (middle), and III (right). Different colors of the tetrahedra indicate different crystallographic Sn positions.

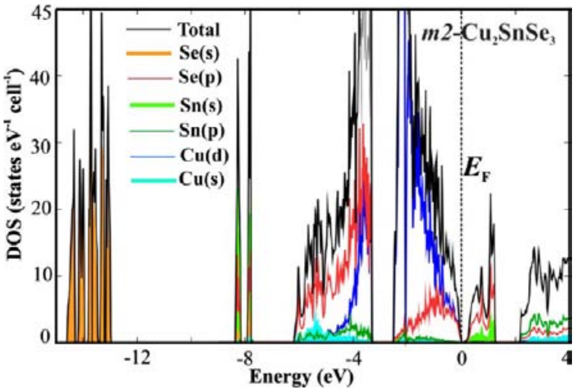

Figure 8. Calculated total electronic density of states of monoclinic-II Cu_2SnSe_3 together with the contributions of relevant atomic states.

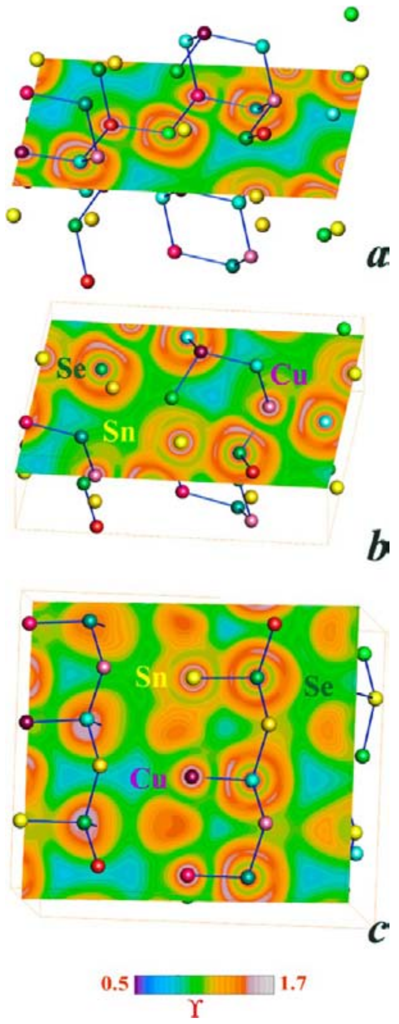

Figure 9. Electron localizability indicator in monoclinic-II Cu_2SnSe_3: (a) ELI-D distribution in the Cu−Se plane; (b) ELI-D distribution around the Sn−Se contacts; (c) comparison of Cu−Se and Sn−Se interactions in the ELI-D distribution.

elements, tin species carry the largest positive and the selenium atoms the largest negative charge, while copper shows an intermediate positive charge. Thus, the charge transfer represents only a part of atomic interactions which are responsible for the organization of the crystal structure of *m2*-Cu_2SnSe_3. The covalent interactions may be analyzed by applying the electron localizability approach. Indeed, analysis of the distribution of the electron localizability indicator in *m2*-Cu_2SnSe_3 reveals maxima of ELI-D between the Se and Cu (Figure 9a) and confirms the direct covalent bonding within the Cu−Se framework. There is also clear ELI-D attractors on the Sn−Se lines (Figure 9b), suggesting the transformation from a lone pair to a bonding character of the atomic interaction in this region of the crystal structure. The ELI-D distribution in the penultimate shells of Cu species slightly deviates from a spherical one (Figure 9b,c). The structuring of the penultimate shell indicates a participation of these electrons in the bonding within the valence region (cf., DOS above). Combining the QTAIM and ELI-D results leads to the conclusion that the atomic framework in *m2*-Cu_2SnSe_3 is formed by covalent polar Cu−Se and Sn−Se bonds.

Thermoelectric Properties. Figure 10 shows the temperature dependence of thermoelectric properties for the *m2*-Cu_2SnSe_3 sample. The positive Seebeck coefficient (Figure 10a) demonstrates its p-type conducting behavior suggesting a very small defect on the Cu site or a small excess of Sn in respect to Se. Within the whole temperature range investigated, the Seebeck coefficient remains almost unchanged, ranging from 344 to 384 $\mu V\ K^{-1}$. These values are larger than 137−275 $\mu V\ K^{-1}$ (ref 1) and around 100−225 $\mu V\ K^{-1}$ (ref 5). The band gap E_g could be estimated as $E_g = 2eS_{max}T(S_{max})$, where S_{max} is the maximum value of Seebeck coefficient, and $T(S_{max})$ is the

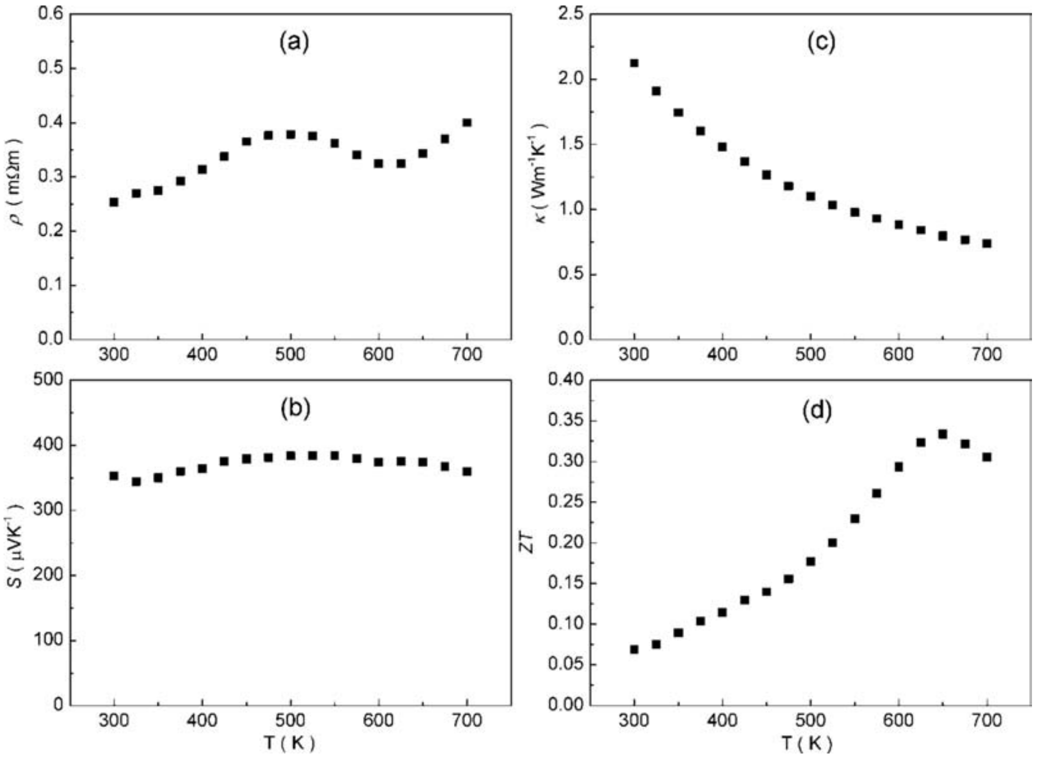

Figure 10. Temperature dependence of (a) the electrical resistivity, (b) Seebeck coefficient, (c) thermal conductivity, and (d) thermoelectric figure of merit *ZT* for an SPS consolidated *m2*-Cu_2SnSe_3 sample.

temperature at which this maximum occurs. With $T(S_{max})$ = 525 K and S_{max} = 384 μV K^{-1}, we get a band gap of 0.4 eV, close to 0.1 eV obtained from the band structure calculation. Figure 10b depicts the relatively large electrical resistivity ρ, varying from 0.25 to 0.40 mΩm. Usually the electrical resistivity monotonically decreases after $T(S_{max})$ because of intrinsic excitation, but an abnormal increase in electrical resistivity above 600 K is observed. This is probably due to Cu vacancy defects which are usually found in Cu-containing selenides, while the influence on Seebeck is more trivial to detect. The confirmation of this assumption and the understanding of the mechanism will be the focus of our future work. Thermoelectric materials are usually narrow band gap semiconductors, whose electrical transport properties are sensitive to composition and could be significantly affected by small deviations from stoichiometry. In Cu-based chalcogenides $Cu_{2+x}Zn_{1-x}SnSe_4$,[35] $Cu_{2+x}Cd_{1-x}SnSe_4$,[36] and $Cu_{2+x}Zn_{1-x}GeSe_4$,[37] the excess of Cu was utilized to increase the carrier concentration and tune electrical transport properties. Our ongoing investigation shows that an excess of Cu in Cu_2SnSe_3 has the same influence. By carefully controlling the composition, the material obtained in this study after SPS densification exhibits also a composition being very close to the stoichiometric one (WDXS yields $Cu_{2.01(1)}Sn_{1.00(0)}Se_{2.99(0)}$). Therefore, the large Seebeck coefficient and electrical resistivity represent rather intrinsic properties of *m2*-Cu_2SnSe_3.

The total thermal conductivity of *m2*-Cu_2SnSe_3 is quite low, decreasing with rising temperature, from 2.12 W m^{-1} K^{-1} at 300 K to 0.74 W m^{-1} K^{-1} at 700 K (Figure 10c). The electronic component to the thermal conductivity (estimated using the Wiedemann–Franz law, $\kappa_e = L_0T/\rho$, with the Lorenz constant $L_0 = 2.0 \times 10^{-8}$ V^2 K^{-2}) was calculated to contribute less than 5% of the total thermal conductivity. On the basis of the calculations for compounds Cu_2ZnSnX_4 (X = S, Se, Te), small energy differences between different polymorphic modifications of these materials were predicted, thus suggesting the coexistence of compositionally similar but crystallographically different phases as one of the possible sources for their low thermal conductivity.[38] Similarly, the coexistence of monoclinic and cubic phase may be one of the factors contributing to the low thermal conductivity of *m2*-Cu_2SnSe_3.

The thermoelectric figure of merit *ZT* of *m2*-Cu_2SnSe_3 is relatively good, reaching 0.33 at 650 K (slightly higher than previously observed[1,6]), even though the carrier concentration is not optimized (Figure 10d).

■ CONCLUSIONS

A new monoclinic-II modification of the ternary compound Cu_2SnSe_3 has been synthesized. The crystal structure of *m2*-Cu_2SnSe_3 was determined through electron diffraction tomography and refined using synchrotron X-ray powder diffraction data. Monoclinic-II is a superstructure to cubic sphalerite-type Cu_2SnSe_3 with an ordered arrangement of Cu and Sn atoms. DTA analysis combined with annealing experiments shows that *m2*-Cu_2SnSe_3 is a low-temperature phase, transforming into the disordered cubic structure above 950 K. According to quantum chemical calculations and confirmed by our experimental results, *m2*-Cu_2SnSe_3 is a narrow-gap semiconductor. Analysis of the chemical bonding applying the electron localizability approach reveals covalent polar Cu–Se and Sn–Se interactions in the crystal structure. A combination of quite large Seebeck coefficient and high electrical resistivity confirms the intrinsic, nearly semiconducting behavior. The thermoelectric figure of merit *ZT* reaches 0.33 at 650 K.

■ ASSOCIATED CONTENT

Ⓢ Supporting Information

Crystallographic information file (CIF) for the synchrotron X-ray powder diffraction data. This material is available free of charge via the Internet at http://pubs.acs.org.

■ AUTHOR INFORMATION

Corresponding Author

*E-mail: grin@cpfs.mpg.de. Phone: +49-351-46464000.

Notes

The authors declare no competing financial interest.

■ ACKNOWLEDGMENTS

The authors thank Dr. W. Schnelle, Dr. H. Borrmann, Mr. S. Hückmann, Dr. Y. Prots, Mrs. S. Scharsach, Mrs. S. Kostmann, Mrs. M. Eckert, Dr. G. Auffermann, Dr. I. Veremchuk, Mr. R. Koban, and Dr. R. Gumeniuk for experimental support and discussions.

■ REFERENCES

(1) Shi, X. Y.; Xi, L. L.; Fan, J.; Zhang, W. Q.; Chen, L. D. *Chem. Mater.* **2010**, *22*, 6029−6031.
(2) Skoug, E. J.; Cain, J. D.; Morelli, D. T. *J. Alloys Compd.* **2010**, *506*, 18−21.
(3) Skoug, E. J.; Cain, J. D.; Morelli, D. T. *J. Electron. Mater.* **2012**, *41*, 1232−1236.
(4) Lu, X.; Morelli, D. T. *J. Electron. Mater.* **2012**, *41*, 1554−1558.
(5) Ibanez, M.; Cadavid, D.; Anselmi-Tamburini, U.; Zamani, R.; Gorsse, S.; Li, W. H.; Lopez, A. M.; Morante, J. R.; Arbiol, J.; Cabot, A. *J. Mater. Chem. A* **2013**, *1*, 1421−1426.
(6) Fan, J.; Liu, H. L.; Shi, X. Y.; Bai, S. Q.; Shi, X.; Chen, L. D. *Acta Mater.* **2013**, *61*, 4297−4304.
(7) Xi, L.; Zhang, Y. B.; Shi, X. Y.; Yang, J.; Shi, X.; Chen, L. D.; Zhang, W.; Yang, J. H.; Singh, D. J. *Phys. Rev. B* **2012**, *86*, 155201.
(8) Palatnik, L. S.; Koshkin, V. M.; Galchinetskii, L. P.; Kolesnikov, V. I.; Komnik, Y. F. *Phys. Solid State* **1962**, *4*, 1052−1053.
(9) Rivet, J.; Laruelle, P.; Flahaut, J. *C. R. Hebd. Seances Acad. Sci.* **1963**, *257*, 161.
(10) Sharma, B. B.; Ayyar, R.; Singh, H. *Phys. Status Solidi A* **1977**, *40*, 691−696.
(11) Hahn, H.; Klingen, W.; Ness, P.; Schulze, H. *Naturwissenschaften* **1966**, *53*, 18.
(12) Rivet, J. *Ann. Chim.* **1965**, *10*, 243.
(13) Delgado, G. E.; Mora, A. J.; Marcano, G.; Rincon, C. *Mater. Res. Bull.* **2003**, *38*, 1949−1955.
(14) Gulay, L. D.; Daszkiewicz, M.; Ostapyuk, T. A.; Klymovych, O. S.; Zmiy, O. F. *Acta Crystallogr., Sect. C* **2010**, *66*, I58−I60.
(15) Kolb, U.; Mugnaioli, E.; Gorelik, T. E. *Cryst. Res. Technol.* **2011**, *46*, 542−554.
(16) Aydemir, U.; Akselrud, L.; Carrillo-Cabrera, W.; Candolfi, C.; Oeschler, N.; Baitinger, M.; Steglich, F.; Grin, Y. *J. Am. Chem. Soc.* **2010**, *132*, 10984−10985.
(17) Carrillo-Cabrera, W. In *Proceedings of EMC2012*, Vol. 2, http://www.emc2012.org.uk/documents/Abstracts/Abstracts/EMC2012_0335.pdf.
(18) Akselrud, L. G.; Y. Z., P.; Grin, Yu.N.; Pecharski, V. K.; Baumgartner, B.; Wölfel, E. *Mater. Sci. Forum* **1993**, *133−136*, 335−340.
(19) Spek, A. L. *J. Appl. Crystallogr.* **2003**, *36*, 7−13.
(20) Jepsen, O.; Burkhardt, A.; Andersen, O. K. *The Program TBLMTO-ASA, Version 4.7*; Max-Planck-Institut für Festkörperforschung: Stuttgart, 1999.
(21) von Barth, U.; Hedin, L. *J. Phys. C* **1972**, *5*, 1629−1642.
(22) Andersen, O. K. *Phys. Rev. B* **1975**, *12*, 3060−3083.
(23) Kohout, M. *Int. J. Quantum Chem.* **2004**, *97*, 651−658.
(24) Wagner, F. R.; Bezugly, V.; Kohout, M.; Grin, Y. *Chem.—Eur. J.* **2007**, *13*, 5724−5741.
(25) Kohout, M. *Faraday Discuss.* **2007**, *135*, 43−54.
(26) Bader, R. F. W. *Atoms in Molecules, A Quantum Theory*; Clarendon Press and Oxford University Press Inc: New York, 1994.
(27) Kohout, M. *Program DGrid 4.6*, 2012.
(28) Marcano, G.; de Chalbaud, L. M.; Rincon, C.; Perez, G. S. *Mater. Lett.* **2002**, *53*, 151−154.
(29) Berger, L. I.; Prochukhan, V. D.; Tybulewicz, A. *Ternary Diamond-Like Semiconductors*; Consultants Bureau: New York, 1969.
(30) Rivet, J.; Laruelle, P.; Flahaut, J.; Fichet, R. *Bull. Soc. Chim. Fr.* **1970**, 1667.
(31) Burla, M. C.; Caliandro, R.; Camalli, M.; Carrozzini, B.; Cascarano, G. L.; Giacovazzo, C.; Mallamo, M.; Mazzone, A.; Polidori, G.; Spagna, R. *J. Appl. Crystallogr.* **2012**, *45*, 357−361.
(32) Sheldrick, G. M. *Acta Crystallogr., Sect. A* **2008**, *64*, 112−122.
(33) Zhai, Y. T.; Chen, S. Y.; Yang, J. H.; Xiang, H. J.; Gong, X. G.; Walsh, A.; Kang, J.; Wei, S. H. *Phys. Rev. B* **2011**, *84*, 075213.
(34) Parthé, E. *Cristallochimie des Structures Tétraédriques*; Gordon & Breach Publishing Group: London, 1972.
(35) Liu, M. L.; Huang, F. Q.; Chen, L. D.; Chen, I. W. *Appl. Phys. Lett.* **2009**, *94*, 202103.
(36) Liu, M. L.; Chen, I. W.; Huang, F. Q.; Chen, L. D. *Adv. Mater.* **2009**, *21*, 3808−3812.
(37) Zeier, W. G.; LaLonde, A.; Gibbs, Z. M.; Heinrich, C. P.; Panthofer, M.; Snyder, G. J.; Tremel, W. *J. Am. Chem. Soc.* **2012**, *134*, 7147−7154.
(38) Sevic, C.; Cagin, T. *Appl. Phys. Lett.* **2009**, *95*, 112105.